Accelerated Nuclear Magnetic Resonance Spectroscopy with Deep Learning

Xiaobo Qu[1*], Yihui Huang[1], Hengfa Lu[1], Tianyu Qiu[1], Di Guo[2], Vladislav Orekhov[3], Zhong Chen[1*]

Nuclear magnetic resonance (NMR) spectroscopy serves as an indispensable tool in chemistry and biology but often suffers from long experimental time. We present a proof-of-concept of harnessing deep learning and neural network for high-quality, reliable, and very fast NMR spectra reconstruction from limited experimental data. We show that the neural network training can be achieved using solely synthetic NMR signal, which lifts the prohibiting demand for large volume of realistic training data usually required in the deep learning approach.

Nuclear magnetic resonance (NMR) spectroscopy is an invaluable biophysical tool in modern chemistry and life sciences. Examples include characterization of complex protein structures[1, 2] and studies disordered[3] and short-lived molecular systems[4]. However, duration of NMR experiments increase rapidly with spectral resolution and dimensionality[5]. Thus, a typical multidimensional protein experiment requires several hours or even weeks[6]. This often imposes unbearable limitations due to low sample stability and/or excessive costs of NMR measurement time. Thus, accelerating data acquisition is a fundamental problem in modern NMR spectroscopy.

To accelerate the data acquisition, in the Non-Uniform Sampling (NUS) acquisition approach, a small fraction of traditional NMR measurements, usually called free induction decay (FID), is augmented with a computational model to reconstruct high quality spectra[5, 7-12]. To achieve good spectra reconstructions, prior knowledge must be incorporated in order to compensate for missing information introduced by the NUS scheme. Representative methods include the maximum entropy[6], spectrum sparsity in compressed sensing[9, 10, 13], spectral line-shape estimation in SMILE[14], tensor structures in MDD[5] or Hankel tensors[11], and exponential nature of NMR signal in low rank[7]. Spectra are reconstructed very well using these approaches. Although these approaches vary in prior knowledge or implementations, they all share a key character: Iterative and computationally demanding reconstruction process that takes much time.

Motivated by the exciting achievements of deep learning (DL)[15], a representative artificial intelligence approach using neural networks, we will explore the end-to-end mapping with DL for the NMR spectra reconstruction, enabling fast and high-quality reconstructions. In contrast to the traditional methods that take advantage of one or more predefined priors for reconstruction, for instance, sparsity and low rank, the proposed DL approach mines the underlying information embedded in data and thus does not require any predefined priors.

A critical challenge of the DL is that it requires an enormous amount of realistic experimental data at the training stage. Whilst obtaining of such a gigantic data set is practically impossible due to the NMR sample and instrument time limitations, our work demonstrates that successful training of the neural network in the DL is possible using solely synthetic data. These are generated using the classic assumption that NMR FID is a superposition of small number of exponential functions[6, 7]. The strategy of using synthetic data for training is beyond the traditional DL approach that requires huge volume of practical data. This work suggests a way for bridging the traditional signal modeling to DL and for enabling smart artificial intelligence computational tools in applications that lack enough practical data to train the neural network. This work can be treated as a proof-of-concept for DL NMR spectroscopy.

Reconstructing a spectrum from NUS data is equivalent to mapping of the input undersampled FID signal to the target spectrum. In the DL NMR, a neural network is trained to perform the mapping as shown in Figure 1. First, the spectrum artifacts introduced by NUS are removed with dense convolutional neural network (CNN) and then intermediately reconstructed spectra are further refined to maintain the data consistency to the sampled signal. Artifacts are gradually removed as the stage of reconstruction increases and the final spectrum is produced after several stages. In this implementation, dense CNN is chosen because it ensures maximum information flow between layers in the neural network[16] while data consistency constraint the reconstruction

[1]Department of Electronic Science, Fujian Provincial Key Laboratory of Plasma and Magnetic Resonance, State Key Laboratory of Physical Chemistry of Solid Surfaces, Xiamen University, Xiamen, China [2]School of Computer and Information Engineering, Xiamen University of Technology, Xiamen 361024, China. [3]Department of Chemistry and Molecular Biology and Swedish NMR Centre, University of Gothenburg, Box 465, Gothenburg 40530, Sweden
Correspondence should be addressed to Xiaobo Qu (quxiaobo@xmu.edu.cn) or Zhong Chen (chenz@xmu.edu.cn).

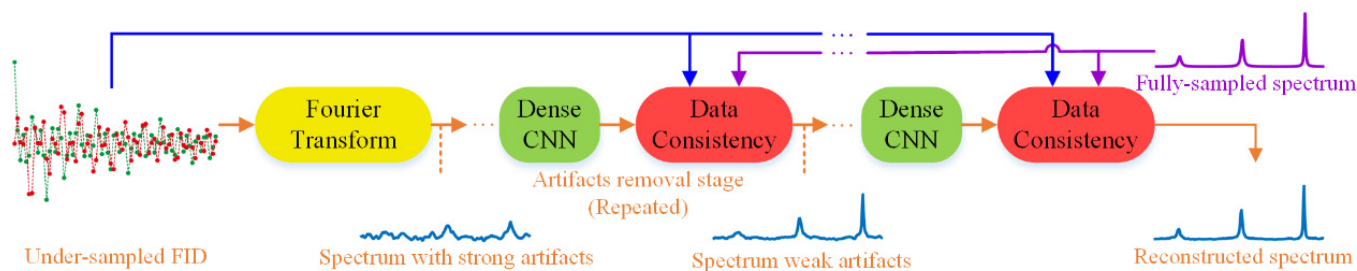subjecting to the sampled data points[17, 18].

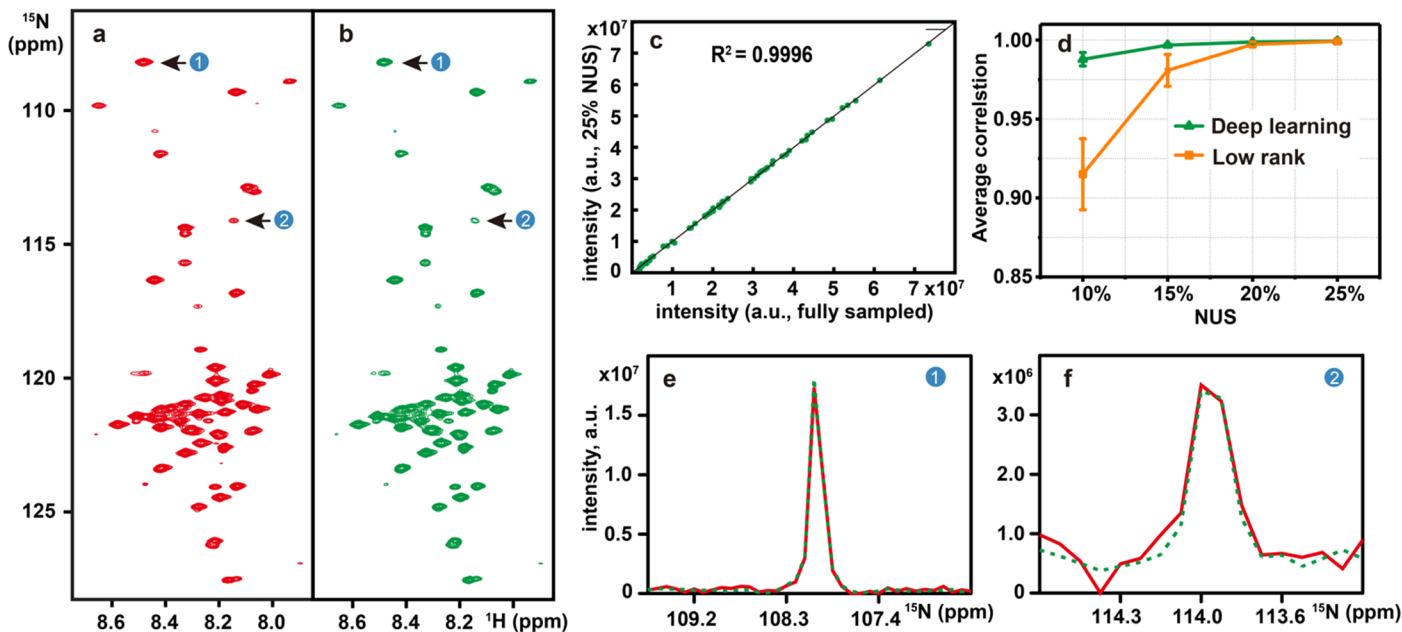Figure 1. Flowchart of deep learning NMR spectroscopy. Note: Please refer to Supplement S1 for more details.

Figure 2. Reconstruction of a 2D ^{1}H–^{15}N HSQC spectrum of the cytosolic domain of CD79b protein from the B-cell receptor. (a) and (b) are the fully sampled spectrum and deep learning NMR reconstruction from 25% NUS data, respectively. (c) Peak intensity correlations between fully sampled spectrum and reconstructed spectrum. (d) denotes the peak intensity correlation obtained with the deep learning and low rank methods under different NUS levels. (e) and (f) are zoomed out 1D ^{15}N traces of (a). Red and green lines represent the reference and the reconstructed spectra, respectively. Note: The R^2 denotes the square of Pearson correlation coefficient. The closer the value of R^2 gets to 1, the stronger the correlation between the reference and the reconstructed spectra is. The average and standard deviations of correlations in (d) are computed over 100 NUS trials.

The key issue for DL NMR is to learn the mapping. We used computer to generate the fully-sampled time domain NMR signal, from which undersampled NUS signal was obtained using Poisson gap sampling scheme (See Supplement S1.1.2 for more details). Given the synthetic NUS signal y and the corresponding target spectrum s produced from the fully sampled time domain data, a large number of pairs (y_k, s_k) (k=1, 2, ..., K) are fed into the neural network to learn the best network parameters θ that minimizes the least errors $e(\theta) = \sum_{k=1}^{K}(f(y_k, \theta) - s_k)^2$. Therefore, DL provides an optimal mapping $f(y, \theta)$ from the input y to the target spectrum in the sense of least square error for all pairs. Then, for a given undersampled FID $\tilde{y}$ from a NUS experiment, a spectrum $\tilde{s}$ is obtained via $\tilde{s} = f(\tilde{y}, \theta)$.

To demonstrate the applicability of the DL NMR, we validate the reconstruction performance on several protein spectra. As shown in Figure 2, DL reconstructs excellent 2D ^{1}H-^{15}N HSQC spectrum from 25% NUS data with correlation of the peak intensity to the fully sampled spectrum reaching 0.9996. Figure

2d indicates that DL is in pair with the state-of-the-art reconstruction techniques[7] in robustness and spectra quality and may even surpass the other methods at low NUS densities. High fidelity of the reconstructed peak shapes is illustrated in Figures 2e and 2f. Using the network with same trained parameters, the correlations greater than 0.98 were also obtained for 2D spectra of three other proteins (See Supplement S2.3). Figure 3 demonstrates high potential of the DL in reconstructing high-quality 3D HNCO spectra. The peak intensity correlation approaching 0.99 for this spectrum (Figure 3e) illustrates the excellent fidelity of the DL reconstruction. Another good example of the DL reconstruction of a 3D HNCACB spectrum is found in Supplement S2.4.

An important advantage of the DL NMR is fast spectra reconstruction due to harnessing of a non-iterative low-complexity neural network algorithm that allows massive parallelization with graphics processing units (GPU). Without compromising the spectra quality (See Supplement S2.2 and S2.3 for detailed comparisons), DL is much faster than other

state-of-the-art methods such as low rank[7] and compressed sensing[10]. The comparisons, shown in Figure 4, indicate that the computational time of spectra reconstructions in DL NMR are orders of magnitude shorter than times needed for the traditional algorithms. Although, training of the network is computationally demanding, it is done only once, whereas all the subsequent reconstructions of the experimental spectra are fast.

In summary, we present the proof-of-concept demonstration of the DL for reconstructing high quality NMR spectra from NUS data. This result opens an avenue for application of DL and possibly other artificial intelligence techniques in biological NMR. Not limited to NMR, we demonstrated that DL can be achieved using purely synthetic training sets. Thus, the exponential function reconstruction may also be valuable to other biomedical imaging tools[19, 20]. Another important feature of the DL is its inherent ability to mine underlying properties of the signal, which may give the DL NMR the upper hand in crucial applications, where it is hard to define a good model for the signal of interest.
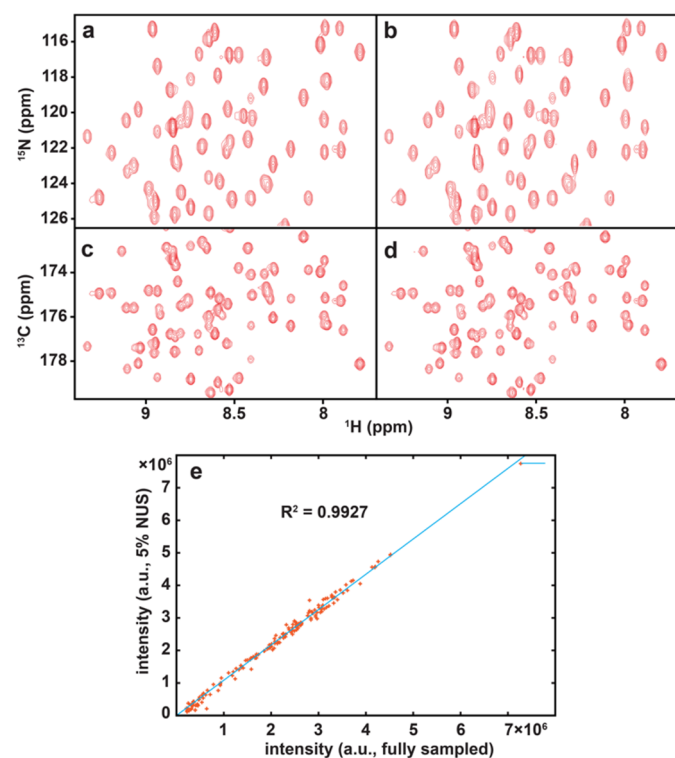

Figure 3. The sub-region of projections on ^{1}H-^{15}N and ^{1}H-^{13}C planes of 3D HNCO spectrum of Azurin 14 kDa protein. (a) and (c) are the projections from the fully sampled spectrum. (b) and (d) projections from the deep Learning reconstruction from 5% NUS data. (e) peak intensity correlation between deep learning reconstructed and fully sampled 3D spectrum.
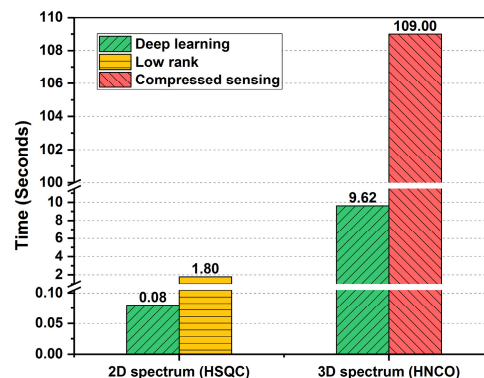

Figure 4. Computational time for the spectra reconstruction with deep learning, low rank and compressed sensing. Experiments were carried out in a dual CPUs (2.2 GHz, 12 cores per CPU) computer server equipped with 128 GB RAM and one Nvidia Tesla K40M. Deep learning, low rank and compressed sensing were implemented in Tensorflow (GPU), MATLAB (CPU) and MddNMR (CPU), respectively. Both low rank and compressed sensing algorithms were accelerated with CPU-based parallel computing in 24 threads. The indirect dimensions of tested 2D spectrum has 256 points while its direct dimension is 116 points. The indirect dimensions of the 3D spectra are 60x60 points, and its direct dimension has 732 points.

References

1. Huang, R., Pérez, F. & Kay, L.E. *Proc. Natl. Acad. Sci. U. S. A.* **114**, E9846 (2017).
2. Sounier, R. et al. *Nature.* **524**, 375 (2015).
3. Chhabra, S. et al. *Proc. Natl. Acad. Sci. U. S. A.* **115**, E1710 (2018).
4. Theillet, F.-X. et al. *Nature.* **530**, 45 (2016).
5. Jaravine, V., Ibraghimov, I. & Yu Orekhov, V. *Nat. Meth.* **3**, 605 (2006).
6. Mobli, M. & Hoch, J.C. *Prog. Nucl. Magn. Reson. Spectrosc.* **83**, 21-41 (2014).
7. Qu, X., Mayzel, M., Cai, J.-F., Chen, Z. & Orekhov, V. *Angew. Chem., Int. Ed.* **54**, 852-854 (2015).
8. Coggins, B.E. & Zhou, P. *J. Biomol. NMR.* **42**, 225-239 (2008).
9. Holland, D.J., Bostock, M.J., Gladden, L.F. & Nietlispach, D. *Angew. Chem., Int. Ed.* **50**, 6548-6551 (2011).
10. Kazimierczuk, K. & Orekhov, V.Y. *Angew. Chem., Int. Ed.* **50**, 5556-5559 (2011).
11. Ying, J. et al. *IEEE Trans. Signal Process.* **65**, 3702-3717 (2017).
12. Robson, S., Arthanari, H., Hyberts, S.G. & Wagner, G. in Methods in Enzymology, Vol. 614. (ed. A.J. Wand) 263-291 (Academic Press, 2019).
13. Shrot, Y. & Frydman, L. *J. Magn. Reson.* **209**, 352-358 (2011).
14. Ying, J., Delaglio, F., Torchia, D.A. & Bax, A. *J. Biomol. NMR.* **68**, 101-118 (2017).
15. LeCun, Y., Bengio, Y. & Hinton, G. *Nature.* **521**, 436 (2015).
16. Huang, G., Liu, Z., Maaten, L.v.d. & Weinberger, K.Q. in *2017 IEEE Conference on Computer Vision and Pattern Recognition (CVPR)* 2261-2269 (IEEE, Honolulu, HI, USA; 2017).
17. Wang, S. et al. in *2016 IEEE 13th International Symposium on Biomedical Imaging (ISBI)* 514-517 (IEEE, Prague, Czech Republic; 2016).
18. Schlemper, J., Caballero, J., Hajnal, J.V., Price, A.N. & Rueckert, D. *IEEE Trans. Med. Imaging.* **37**, 491-503 (2018).
19. Durand, A. et al. *Nat. Commun.* **9**, 5247 (2018).
20. Zhu, B., Liu, J.Z., Cauley, S.F., Rosen, B.R. & Rosen, M.S. *Nature.* **555**, 487 (2018).

Author contributions

Competing interests

Supplement S1: Methodology

In the following, we first illustrate the detailed architectures (Fig. S1-1) of the deep learning (DL) NMR and then explain each processing parts separately, following the processing of data flow.
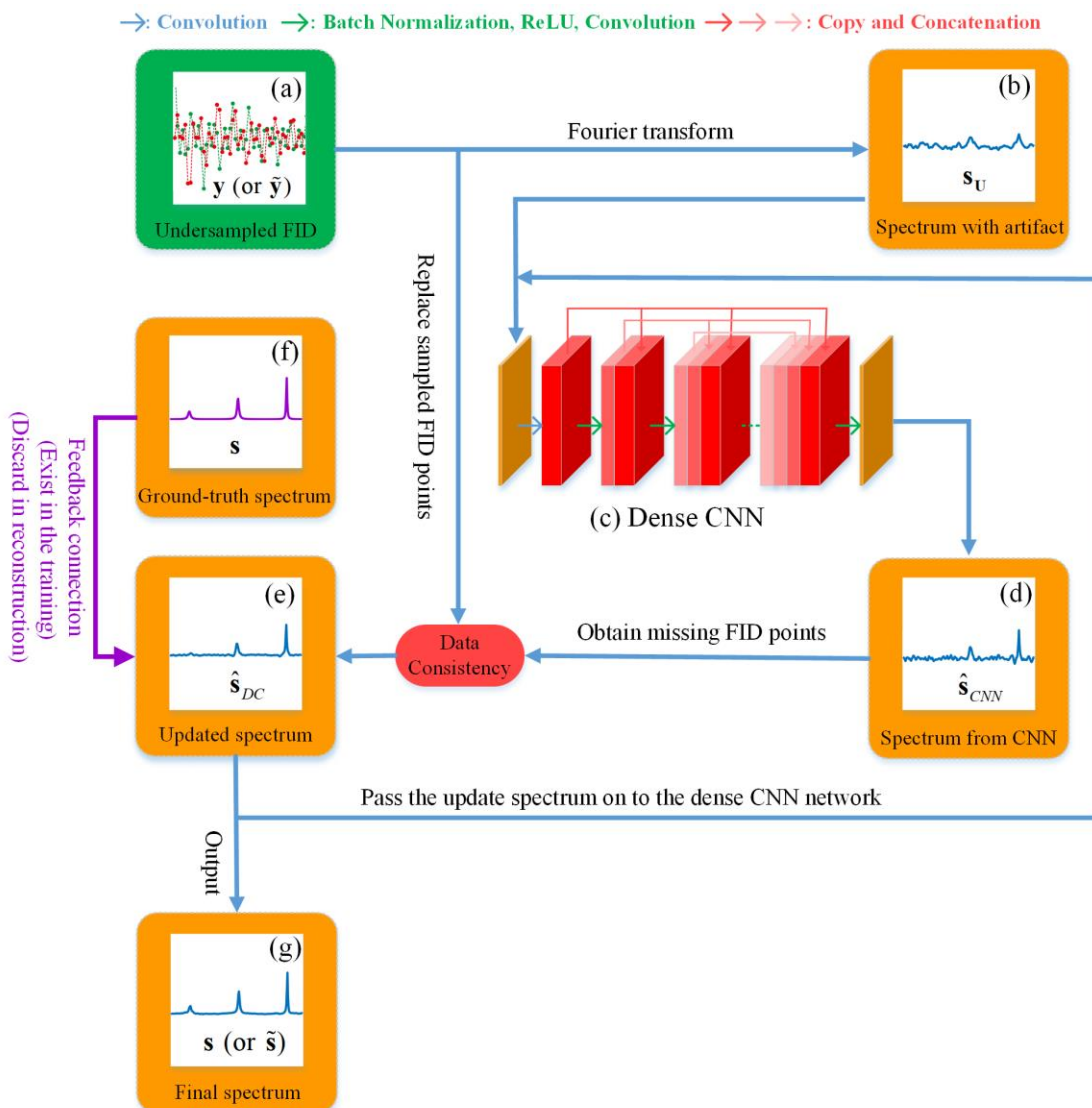

Figure S1-1. The detailed architectures of DL NMR. (a) The undersampled FID, (b) the spectrum with strong artifacts, (c) dense CNN, (d) the output of dense CNN, (e) the updated spectrum from data consistency, (f) fully sampled spectrum, (g) the output of the whole network. Note: The green and orange blocks denote signals in time and frequency domains, respectively. Signals or modules that are marked with the purple color are only existed in the training phase.

The implementation of DL NMR includes two phases, training phase and prediction phase. In the training phase, with the computer-simulated undersampled FID $\mathbf{y}$ to the target spectrum $\mathbf{s}$, a large number of FID/spectrum pairs $(\mathbf{y}_k, \mathbf{s}_k)(k = 1, 2, \cdots, K)$ are input into the neural network to learn the best network parameters $\hat{\boldsymbol{\theta}}$. In the reconstruction phase, given an undersampled FID $\tilde{\mathbf{y}}$ acquired in the NUS experiment, a spectrum $\tilde{\mathbf{s}}$ is obtained via $\tilde{\mathbf{s}} = f(\tilde{\mathbf{y}}, \hat{\boldsymbol{\theta}})$ where f is the trained mapping from undersampled FIDs to spectra. Both training and reconstruction phases are detailed illustrated in the following.

1.1 Training phase

1.1.1 Generate the fully sampled spectrum and the undersampled FID

Our method solely uses the synthetic data as training data, which is significantly different from many deep learning approaches that utilize the realistic data as training data. The fully sampled spectrum satisfies $\mathbf{s} = \mathbf{Fx}$, where $\mathbf{F}$ is the Fourier transform and $\mathbf{x}$ is the fully sampled FID, and the undersampled FID obeys $\mathbf{y} = \mathbf{Ux}$, where $\mathbf{U}$ is the undersampling operator, are generated as follows:

The fully sampled FID $\mathbf{x}$ is simulated according to the classical exponential function modeling as[1-5]:

$$x_n = \sum_{j=1}^{J} \left(A_j e^{i\phi_j} \right) e^{-\frac{n\Delta t}{\tau_j}} e^{in\Delta t 2\pi\omega_j} \quad , \tag{S1-1}$$

where J is the number of exponentials, A_j, ϕ_j, τ_j and f_j are the amplitude, phase, decay time and frequency, respectively, of the jth exponential. By varying these parameters according to Table S1-1, there are 40000 FIDs are simulated.

For each fully sampled FID $\mathbf{x}$, a corresponding under-sampling operator $\mathbf{U}$ is generated following the Poisson-gap sampling scheme[6]. Let k denote the kth sampling trial, then multiple pairs of $(\mathbf{y}_k, \mathbf{s}_k)$ $(k = 1, 2, \cdots, K)$, composed of the undersampled FID $\mathbf{y}_k$ and the fully sampled spectrum $\mathbf{s}_k$, are formed and used to train the neural network. In this work, we simulate $K=40000$ pairs.

Table S1-1. Parameters for 1D synthetic FID

Parameters	Number of Peaks (J)	Amplitude (A)	Frequency (ω)	Decay time (τ)	Phase (ϕ)
Minimum	1	0.05	0.01	10	0
Increment	1	continuous	continuous	continuous	continuous
Maximum	10	1	0.99	179.2	2π

Note: The FID is normalized so that the maximal magnitude of each spectrum is 1.

1.1.2 Generate the initial spectrum from the undersampled FID

The initial spectrum that inputs the neural network is computed as $\mathbf{s}_\mathbf{U} = \mathbf{F}^H \mathbf{U}^T \mathbf{y}$, where $\mathbf{U}^T$ is the adjoint operator of $\mathbf{U}$ and $\mathbf{F}^H$ is the forward Fourier transform. This initial spectrum is with strong artifacts since those unsampled FID data are filled with zeros on non-acquired positions.

Since an undersampled FID $\mathbf{y}_k$ corresponds to one NUS sampling $\mathbf{U}_k$, thus the generated initial spectrum will be $\mathbf{s}_{\mathbf{U}_k} = \mathbf{F}^H \mathbf{U}_k^T \mathbf{y}_k$ $(k = 1, 2, \cdots, K)$ and $K=40000$ in the implementation.

1.1.3 Reduce spectrum artifacts with dense neural network

The spectrum $\mathbf{s}_\mathbf{U}$ is fed into the densely connected convolutional neural networks (Fig.S1-1(c)), known as dense CNN [6]. This neural network learns a map f_{CNN} to reduce the spectrum artifact and yield the 'clean' spectrum denoted as $\hat{\mathbf{s}}_{CNN}$.

The structures of dense CNN (Fig. S1-1(c)) include 8 convolutional layers. Between adjacent layers of dense CNN, there exists the batch normalization followed by the ReLU activation function. With the initial spectrum as input, first convolutional layer produces 16 spectra while the rest of convolutional layers each output 12 spectra except for the last layer which provides only one spectrum - the spectrum $\hat{\mathbf{s}}_{CNN}$. The lth $(2 \leq l \leq 8)$ layer takes outputs of preceding $(l\text{-}1)^{\text{th}}$ layers, i.e., $16+12\times(l\text{-}2)$ spectra.

1.1.4 Enforce the spectrum to maintain data consistency

A data consistency module is incorporated to ensure reconstructed spectra are aligned to acquired data. Given the output of dense CNN $\hat{\mathbf{s}}_{CNN}$, the spectrum is modified as

$$\hat{\mathbf{s}}_{DC} = \arg\min_{\mathbf{s}_{DC}} \left\{ \left\| \mathbf{s}_{DC} - \hat{\mathbf{s}}_{CNN} \right\|^2 + \lambda \left\| \mathbf{y} - \mathbf{U}\mathbf{F}^T\mathbf{s}_{DC} \right\|^2 \right\}, \tag{S1-2}$$

where $\left\| \cdot \right\|$ denotes the norm of a vector, $\mathbf{F}^T$ the inverse Fourier transform, $\mathbf{s}_{DC}$ the underlying spectrum to be optimized, and $\hat{\mathbf{s}}_{DC}$ is the output of data consistency module. A closed form solution of Eq. (S1-2) is

$$\hat{\mathbf{s}}_{DC} = \mathbf{F}\left(\lambda \mathbf{U}^T\mathbf{U} + \mathbf{1} \right)^{-1} \left(\lambda \mathbf{U}^T\mathbf{y} + \mathbf{F}^T\hat{\mathbf{s}}_{CNN} \right), \tag{S1-3}$$

where $\mathbf{1}$ is an identity matrix and $(\cdot)^{-1}$ denotes the inverse of a matrix. Let the FID of $\hat{\mathbf{s}}_g$ be $\hat{\mathbf{x}}_g = \mathbf{F}^T\hat{\mathbf{s}}_g$, then Eq. (S1-3) is equivalent to the following relationship

$$\left(\hat{\mathbf{x}}_{DC} \right)_n = \begin{cases} \left(\mathbf{F}\hat{\mathbf{s}}_{CNN} \right)_n & ,n \notin \Omega \\ \dfrac{\left(\mathbf{F}\hat{\mathbf{s}}_{CNN} \right)_n + \lambda \mathbf{y}_n}{1+\lambda} & ,n \in \Omega \end{cases}, \tag{S1-4}$$

where Ω is the set of positions for sampled FID and n is the index of the FID. The Eq. (S1-4) implies that the FID at the location of sampled data points should be balanced between the acquired data points in the initial data $\mathbf{y}$ and the predicted data point obtained with the dense CNN.

For simplicity, we rename the data consistency as a linear function

$$\hat{\mathbf{s}}_{DC} = f_{DC}\left(\hat{\mathbf{s}}_{CNN}, \mathbf{y} \right), \tag{S1-5}$$

that maps the input $\left(\hat{\mathbf{s}}_{CNN}, \mathbf{y} \right)$ to the spectrum according to Eq. (S1-3). In our implementation, we choose $\lambda = 10^6$ which works well for all the tested spectra.

In this implementation, the two modules described in S1.1.3 and S1.1.4 are combined as one reconstruction stage. As shown in Fig. S1-2, spectrum artifacts (Fig. S1-2(b)) are firstly removed by the dense CNN (Fig. S1-2(c)) in some degree and then the spectrum (Fig. S1-(d)) quality is enhanced by enforcing the data consistency. Further improvement of spectra (Figs. S2-(d)(f)(h)(j)(l)) are retained by repeating reconstruction stage in multiple times.
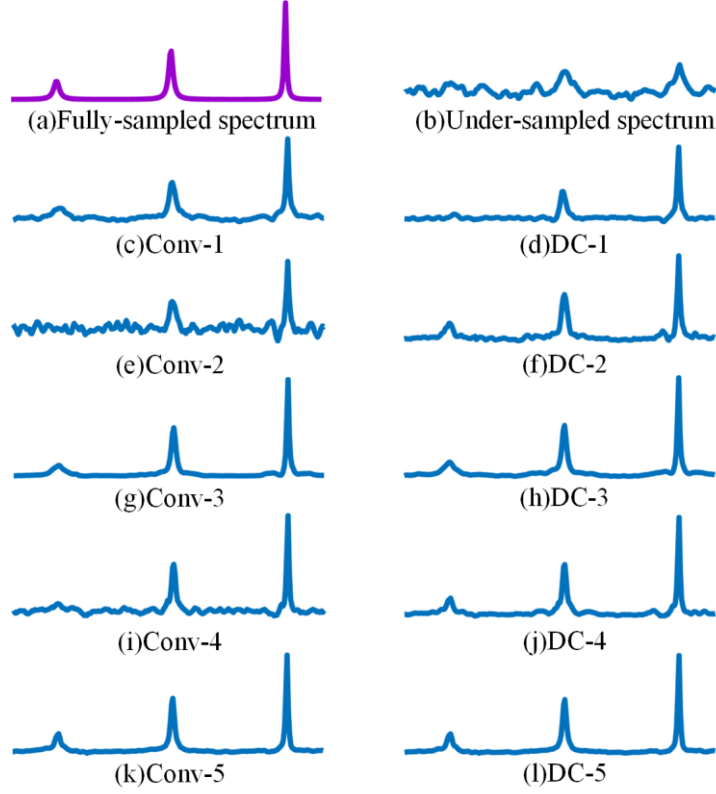
Figure S1-2. The illustrative results of dense CNN and data consistency. Note: *Conv*, *DC*, and the *number (1, 2, 3, 4, 5)* denote the outputs of dense CNN and data consistency, and the order of reconstruction stage, respectively. The final output of the network is (l) DC-5.

1.1.5 Loss function and trained optimal parameters

Let the superscript number q denotes the qth reconstruction stage, then the output at the qth stage is the same as the output of the data consistency module, meaning that $\hat{\mathbf{s}}^q = \hat{\mathbf{s}}^q_{DC}$. The overall loss function in our implementation is

$$\min_{\boldsymbol{\theta}=\{\theta^1,\cdots\theta^q\cdots,\theta^Q\}} \sum_{k=1}^{K}\sum_{q=1}^{Q}\left\|\mathbf{s}_k - \hat{\mathbf{s}}^q_k\left(\theta^q\right)\right\|, \tag{S1-6}$$

where $\boldsymbol{\theta}$ is network parameters to be trained, k denotes the kth NUS trial, which is also equal to the number of FIDs. In the implementation, ADAM scheme is adopted to solve Eq. (S1-5)[7]. Therefore, the optimal parameters $\hat{\boldsymbol{\theta}}$ is obtained by minimizing the output of the network for all training data.

1.2 Reconstruction phase

In the reconstruction phase, given an undersampled FID $\tilde{\mathbf{y}}$ acquired in the NUS experiment, a spectrum $\tilde{\mathbf{s}}$ is reconstructed according to

$$\tilde{\mathbf{s}}=f\left(\tilde{\mathbf{y}},\hat{\boldsymbol{\theta}}\right), \tag{S1-7}$$

where f is the functions that models the whole processing in the neural network.

One thing should be mentioned is that the feedback connection (purple line in Fig. S1-1) is discarded in the reconstruction since the fully sampled FID is not available in practice.

Supplement S2: Other Spectra Results

In the following, all non-uniform sampling tables are generated according to Poisson-gap sampling[8].

The proposed deep learning (DL) approach will be compared with two state-of-the-art NMR spectroscopy reconstruction approaches, including low rank (LR)[2] and compressed sensing (CS)[9-11]. In reconstruction of 2D NMR, CS[10] is excluded since the LR[2] has been shown to outperform the CS. Thus, comparing deep learning (DL) with LR is enough to demonstrate the advantage of DL. In the reconstruction of 3D NMR, CS[10] is included but LR[2] is excluded because the former can handle the realistic 3D NMR data while the latter cannot accomplish this yet.

2.1 Experiments Setup

The important spectra parameters, including four 2D spectra and two 3D spectra, are listed in Table S2-1. More details could be found in below experimental descriptions (S2.1.1 and S2.1.2). The direct dimension of all spectra was processed in NMRPipe[12] before performing reconstructions.

Table S2-1. Important parameters of used spectra.

	Type	Protein name	Protein size	Spectrometer frequency	Size(s) of indirect dimension(s)	References
2D spectra	HSQC	Cytosolic CD79b	~5.7 kDa	800 MHz	256	Figure S2-1
	HSQC	Ubiquitin	~8.6 kDa	800 MHz	98	Figure S2-3
	HSQC	Gb1	~6.3 kDa	600 MHz	150	Figure S2-4
	TROSY	Ubiquitin	~8.6 kDa	800 MHz	128	Figure S2-5
3D spectra	HNCO	Azurin	14 kDa	800 MHz	60×60	Figure S2-7
	HNCACB	GB1-HttNTQ7	2.7 kDa	700 MHz	90×44	Figure S2-9

2.1.1 2D Spectra

We used the same 2D ^{1}H–^{15}N HSQC spectrum (Fig. S2-1) of cytosolic CD79b protein as was described in our previous work[2, 13]. In brief, the spectrum was acquired for 300 μM ^{15}N-^{13}C labeled sample of cytosolic CD79b in 20 mM sodium phosphate buffer, pH 6.7 at 25 °C on 800 MHz Bruker AVANCE III HD spectrometer equipped with 3 mm TCI cryoprobe.

The 2D ^{1}H–^{15}N HSQC spectrum (Fig. S2-3) was acquired from ubiquitin sample at 298.2K temperature on an 800 MHz Bruker spectrometer. Data were recorded with 8 transients and the recycle delay of 1 s.

The 2D ^{1}H–^{15}N HSQC spectra (Fig. S2-4) of GB1 was the data courtesy of Drs. Luke Arbogast and Frank Delaglio at National Institute of Standards and Technology, Institute for Bioscience and Biotechnology Research, USA. The sample was 2 mM U-^{15}N, 20%-^{13}C GB1 in 25 mM PO4, pH 7.0 with 150 mM NaCl and 5% D$_2$O. Data was collected using a phase-cycle selected HSQC at 298 K on a Bruker Advance 600 MHz spectrometer using a room temp HCN TXI probe, equipped with a z-axis gradient system.

The 2D ^{1}H–^{15}N best-TROSY spectrum (Fig. S2-5) of ubiquitin was acquired at 298.2K temperature on an 800 MHz Bruker spectrometer. The spectrum was recorded with 2 transients, the recycle delay of 0.2s.

2.1.2 3D Spectra

The 3D HNCO spectrum obtained from the 800 MHz spectrometer on ^{15}N-^{13}C-labeled Cu(I) azurin sample was described earlier[14].

The 3D HNCACB spectrum (Fig. S2-9) was the data courtesy of Drs. Marius Clore and Samuel Kotler at Laboratory of Chemical Physics, National Institute of Diabetes and Digestive and Kidney Diseases, National Institutes of Health, Bethesda, MD 20892-0520. The data was recorded at 298 K on a Bruker Advance HD 700 MHz spectrometer using a cryogenic TCI probe, equipped with a triple-axis gradient accessory, and was described in previous paper[15].

2.2 Reconstructed 2D HSQC Spectrum of CD79b

Details about the spectrum could be found in Table S2-1. The deep learning method, DL NMR, is compared with a representative NUS NMR reconstruction method, the LR approach[2].

The DL NMR achieves the same level of reconstructed spectra quality as LR method does (at the NUS rate of 25% in Fig. S2-1). The peak intensity correlation values of both methods approaching 0.9999 and representative peak shapes closing to the fully sampled peak shapes can demonstrate this (Figs. S2-1(d)-(g)). At the lower the NUS levels (10% and 15% in Fig. 2(d)), the DL NMR provides higher correlation values as well as lower dispersion of correlation coefficients over 100 NUS trials. The higher quality of the DL NMR reconstruction at low NUS rate is also illustrated in Figs. S2-2(a) and 2(b). These observations imply that DL allows more significant saving of measurement time than the LR method, and also is more robust under different NUS trials, leading to more stable reconstruction.
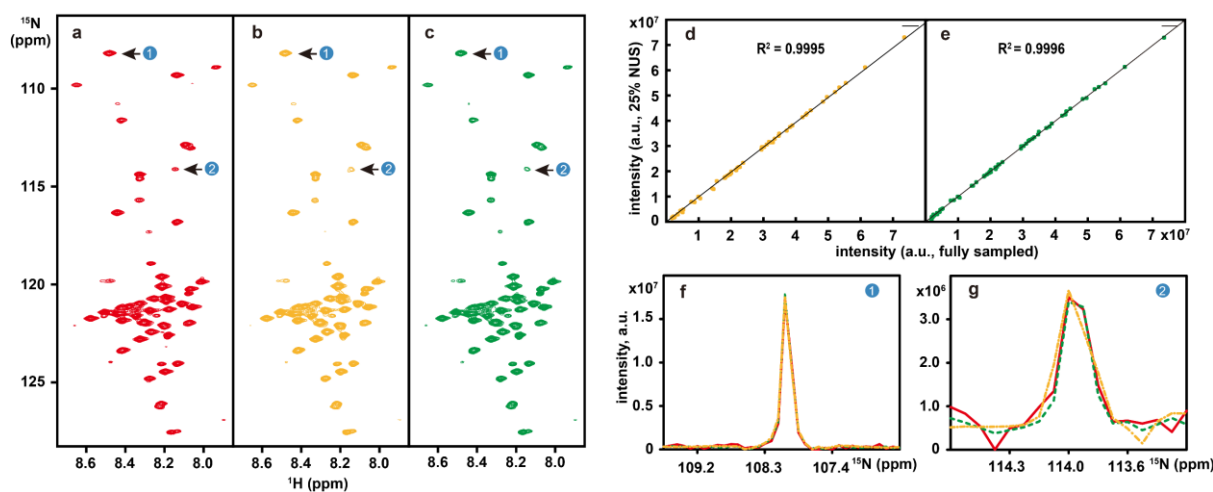

Figure S2-1. Reconstruction of a 2D ^{1}H–^{15}N HSQC spectrum of cytosolic CD79b protein from the B-cell receptor. (a)-(c) are the fully sampled spectra, LR and DL reconstructions from 25% NUS data, respectively; (d) and (e) are peak intensity correlations obtained by LR and DL methods, respectively; (d) and (e) are zoomed out 1D ^{15}N traces, and the red, yellow and green lines represent the spectra obtained with fully-sampling, LR and DL methods, respectively. Note: 25% NUS data were used in the reconstruction.
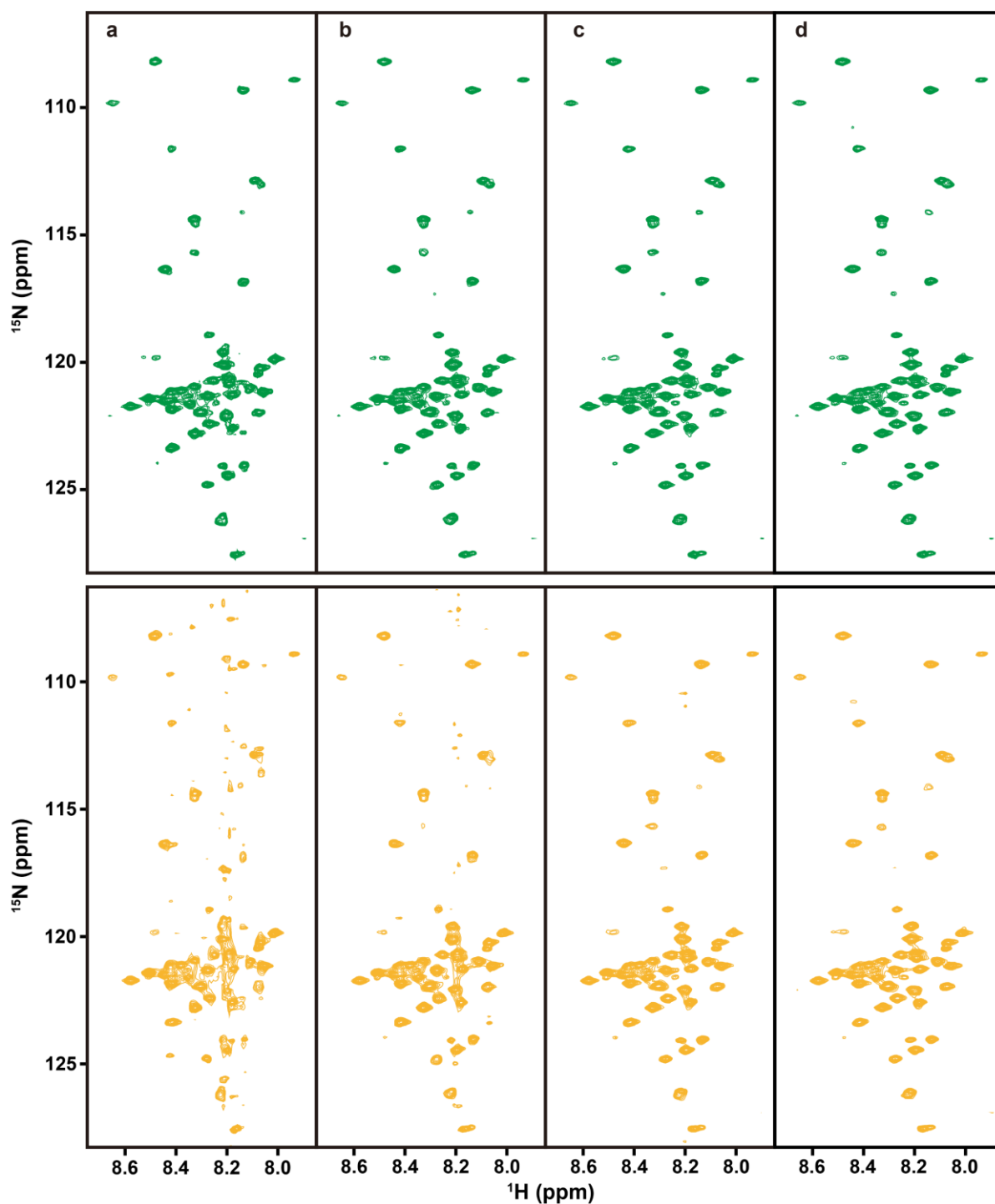
Figure S2-2. Reconstructed 2D ^{1}H-^{15}N HSQC spectra under different amounts of NUS data. (a)-(d) are the reconstructions at NUS of 10%, 15%, 20% and 25%, respectively. The spectra marked with green and yellow colors are reconstructions with DL and LR methods, respectively.

2.3 Other 2D Spectra Reconstruction

To demonstrate the applicability of trained neural networks, we reconstruct another three spectra, including the 2D HSQC spectrum from ubiquitin (Fig. S2-3), the 2D HSQC spectrum from GB1 (Fig. S2-4) and the 2D TROSY spectrum from ubiquitin (Fig. S2-5), details about spectra could be found in Table S2-1.

Both DL and LR methods obtain very high peak intensity correlation (>0.98), which is also confirmed

with almost the same peak shapes to the fully sampled spectra (at the NUS rate of 25%). With fewer data, indicating higher acceleration factors of data acquisition, Fig. S2-6 shows that DL outperforms LR in terms of higher intensity correlations.
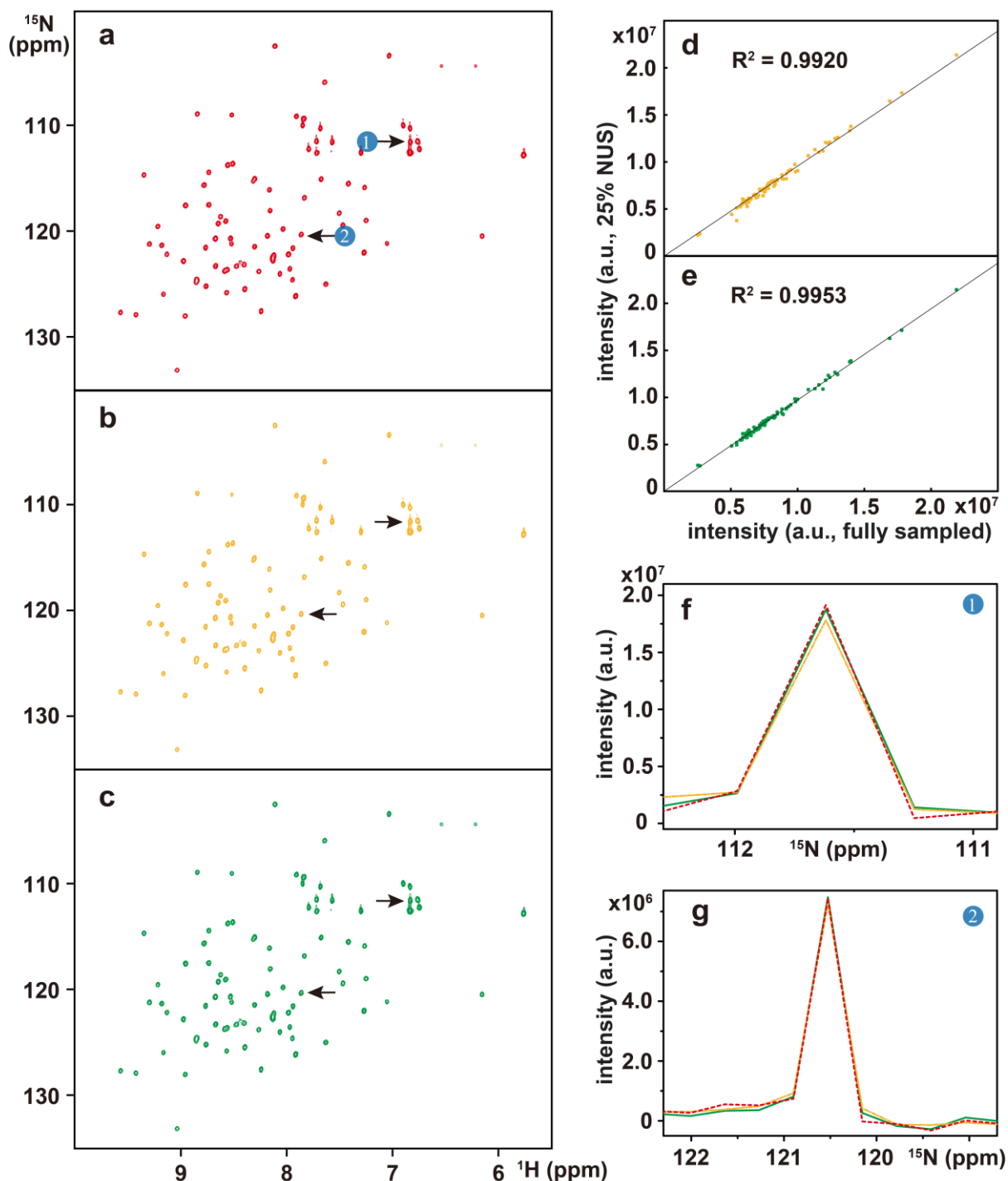

Figure S2-3. Reconstruction of the 2D ^{1}H-^{15}N HSQC spectrum of ubiquitin. (a) is the fully sampled reference spectrum, (b) and (c) are reconstructed spectra from 25% NUS data by LR and DL methods, respectively, (d) and (e) are the peak intensity correlations achieved by LR and DL methods, respectively, (f) and (g) are zoomed out 1D ^{15}N traces, and the red, yellow and green lines represent the reference, LR and DL reconstructed spectra, respectively.
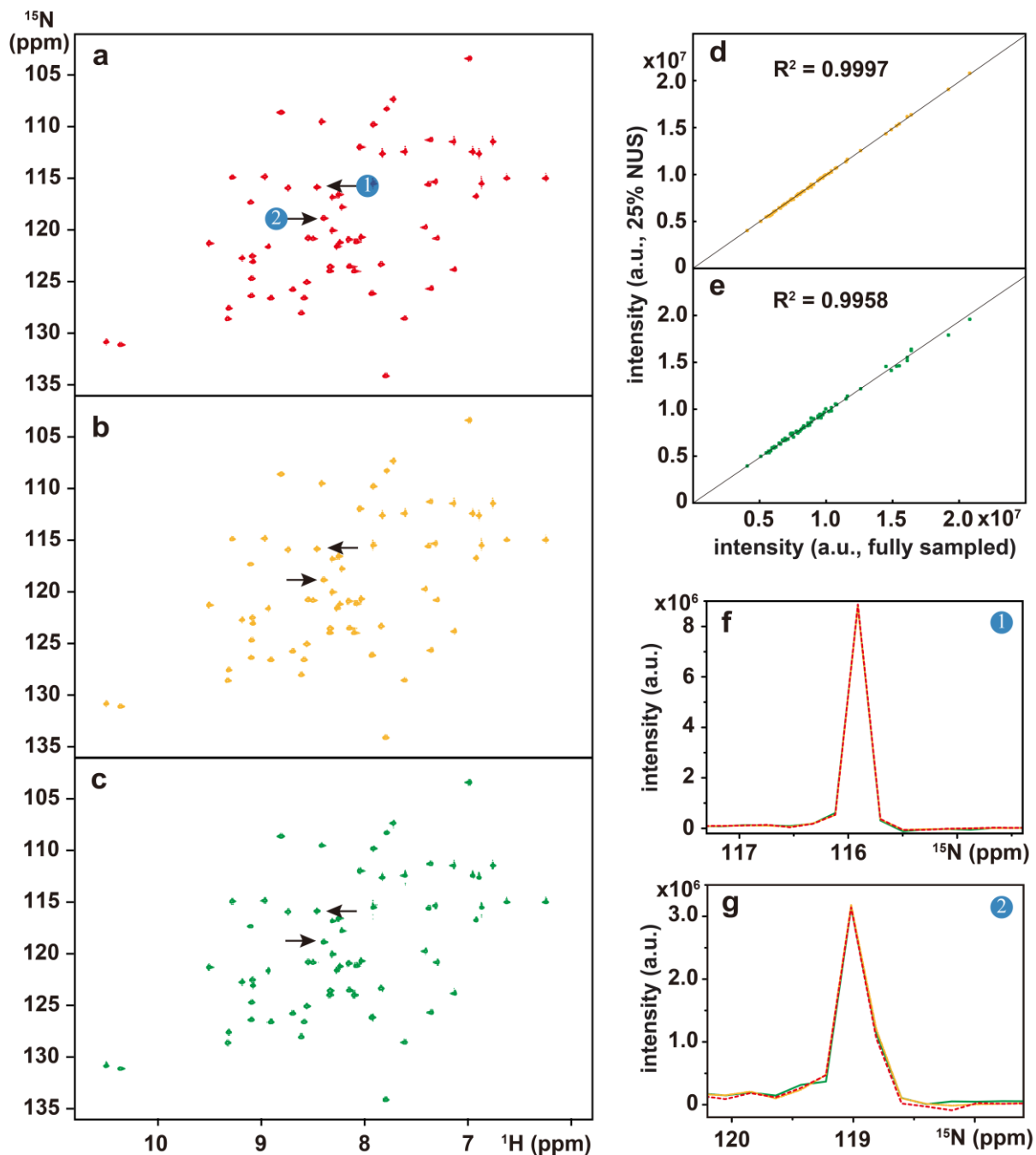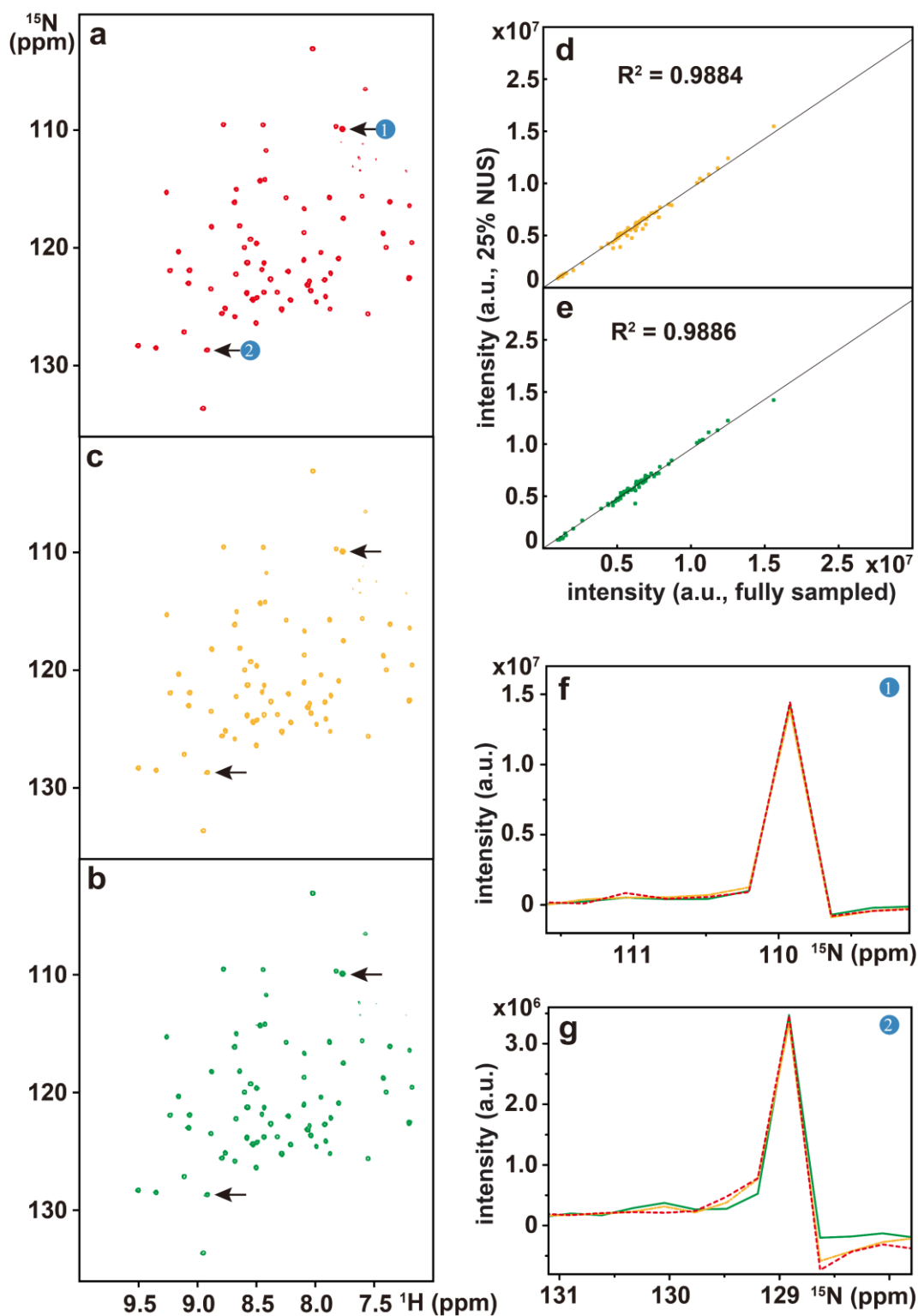
Figure S2-4. Reconstruction of 2D HSQC spectra of GB1. (a) is the fully sampled reference spectrum, (b) and (c) are reconstructed spectra from 25% NUS data by LR and DL methods, respectively, (d) and (e) are the peak intensity correlations achieved by LR and DL methods, respectively, (f) and (g) are zoomed out 1D ^{15}N traces, and the red, yellow and green lines represent the reference, LR and DL reconstructed spectra, respectively.

Figure S2-5. Reconstruction of the 2D ^{1}H-^{15}N best-TROSY spectrum of ubiquitin. (a) is the fully sampled reference spectrum, (b) and (c) are reconstructed spectra from 25% NUS data by LR and deep NMR, respectively, (d) and (e) are the peak intensity correlations achieved by LR and DL methods, respectively, (f) and (g) are zoomed out 1D ^{15}N traces, and the red, yellow and green lines represent the reference, LR and DL NMR reconstructed spectra, respectively.
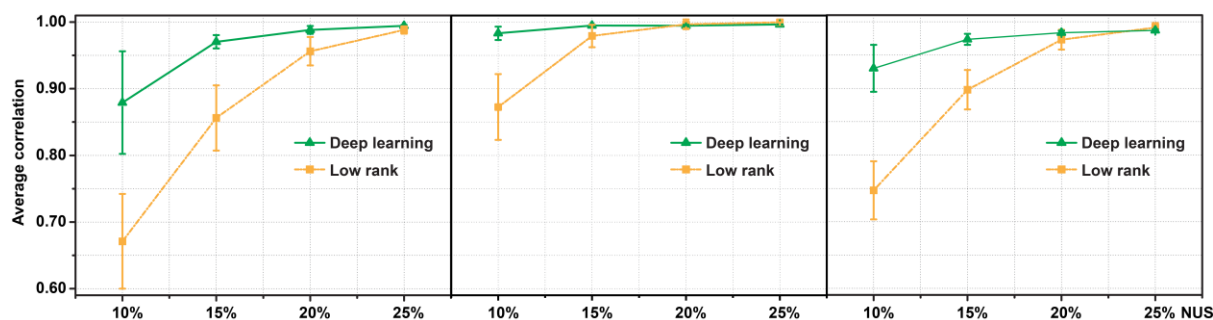
Figure S2-6. Correlation coefficients for the (a) Fig. S2-3, (b) Fig. S2-4 and (c) Fig. S2-5 spectra at different rates of NUS. Note: The green and yellow lines indicate the Pearson correlation coefficient R^2 of DL and LR methods, each compared with the fully sampled spectrum, respectively. The error bars are the standard deviations of the correlations over 100 NUS resampling trials.

2.4 3D Spectra Reconstruction

In this section, we will demonstrate the applicability of the DL NMR method in 3D NMR reconstruction. The 3D spectra include HNCO and HNCACB spectra with details listed in Table S2-1. The state-of-the-art CS[10] reconstruction method is adopted for comparison.

As can be seen in Figs. S2-7, S2-9 and S2-10, both DL and CS approaches produces nice reconstructions of 3D spectra that are very closing to the fully sampled spectra. The peak intensity correlations of DL and CS, with $R^2 > 0.99$, shows the high fidelity of reconstruction (Figs. S2-8 and S2-11).
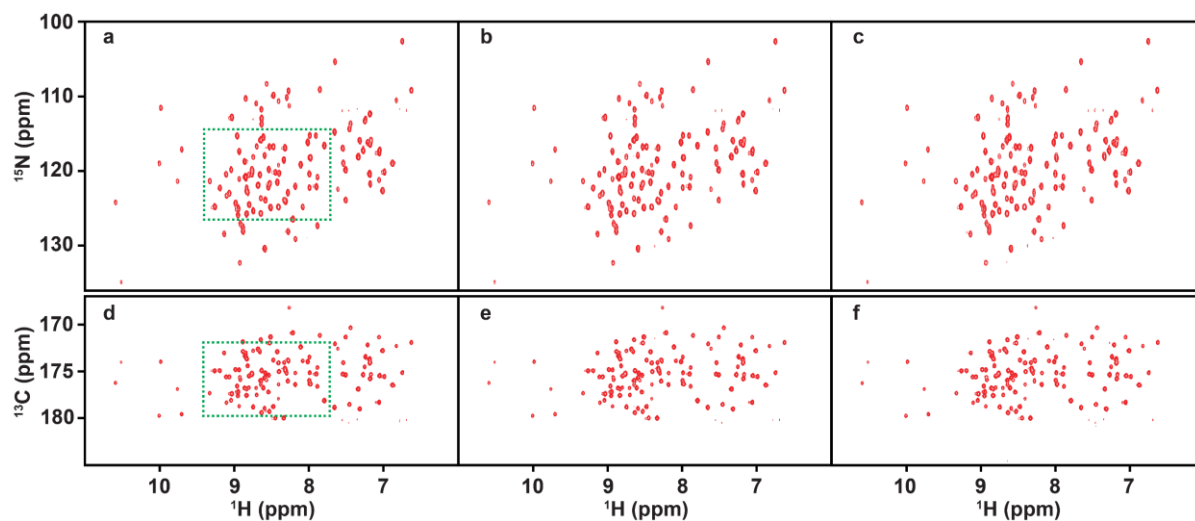

Figure S2-7. The projections on ^{1}H-^{15}N and ^{1}H-^{13}C planes of the 3D HNCO spectra of azurin. (a) and (d) are projection spectra of the fully sampled referenced spectrum. (b) and (e) are projection spectra of the CS reconstructed spectrum. (c) and (f) are projection spectra of the DL reconstructed spectrum. Note: 5% NUS data were acquired for reconstruction. The sub-region of projections marked with green dash rectangle was shown in Fig. 3 in the main text.
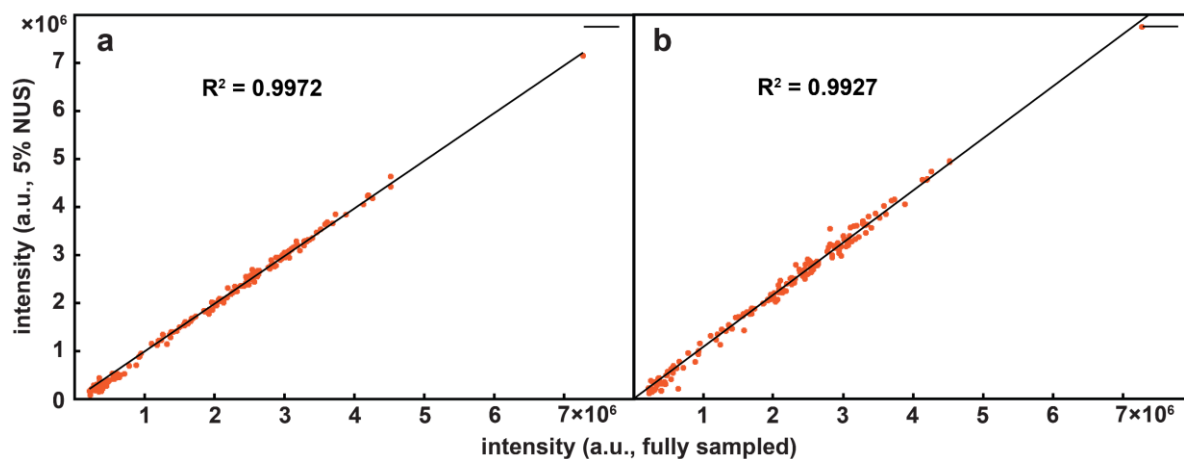
Figure S2-8. Correlation coefficients between reconstructed spectra and fully sampled 3D HNCO shown in Fig. S2-7. (a) and (b) are the peak intensity correlations achieved by CS and DL, respectively.
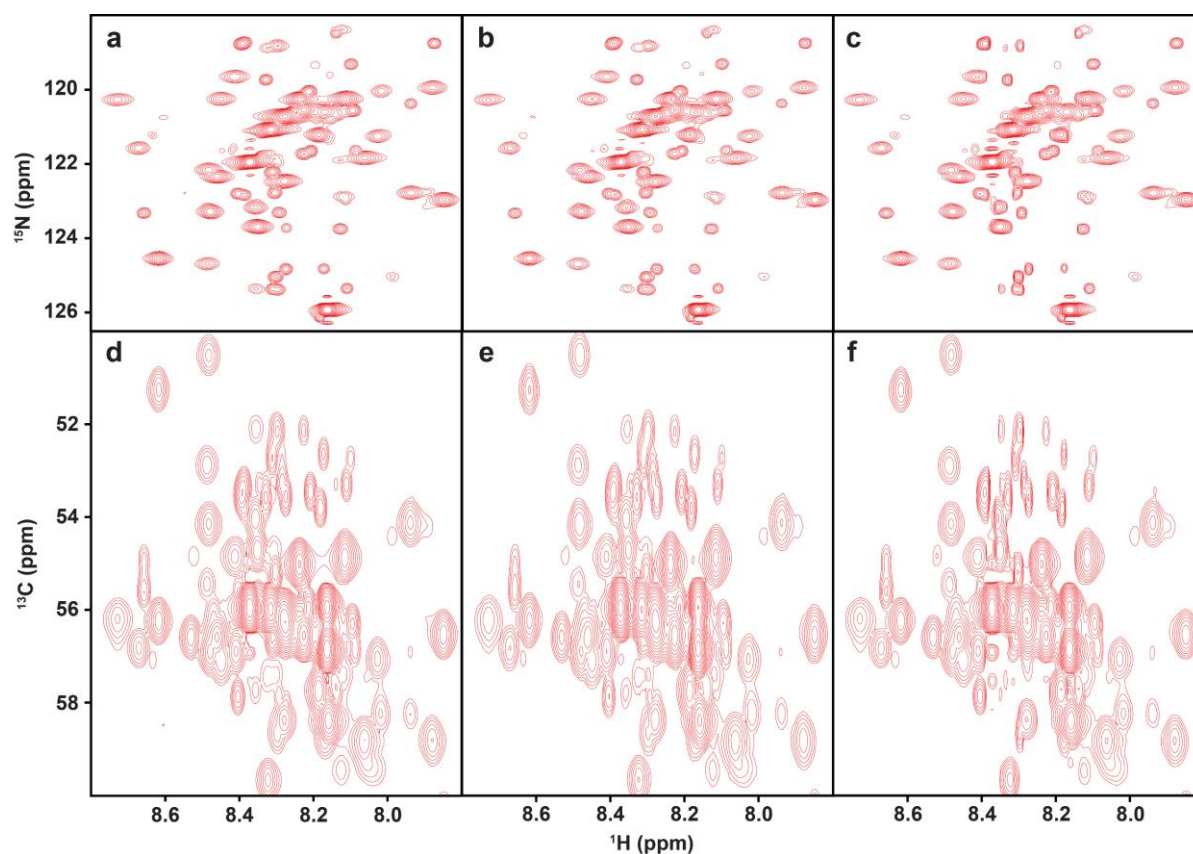

Figure S2-9. The sub-region of the projections on ^{1}H-^{15}N and ^{1}H-^{13}C planes of the 3D HNCACB. (a) and (d) are projection spectra of the fully sampled referenced spectrum. (b) and (e) are projection spectra of the CS reconstructed spectrum. (c) and (f) are projection spectra of the DL reconstructed spectrum. Note: 10% NUS data were acquired for reconstruction.
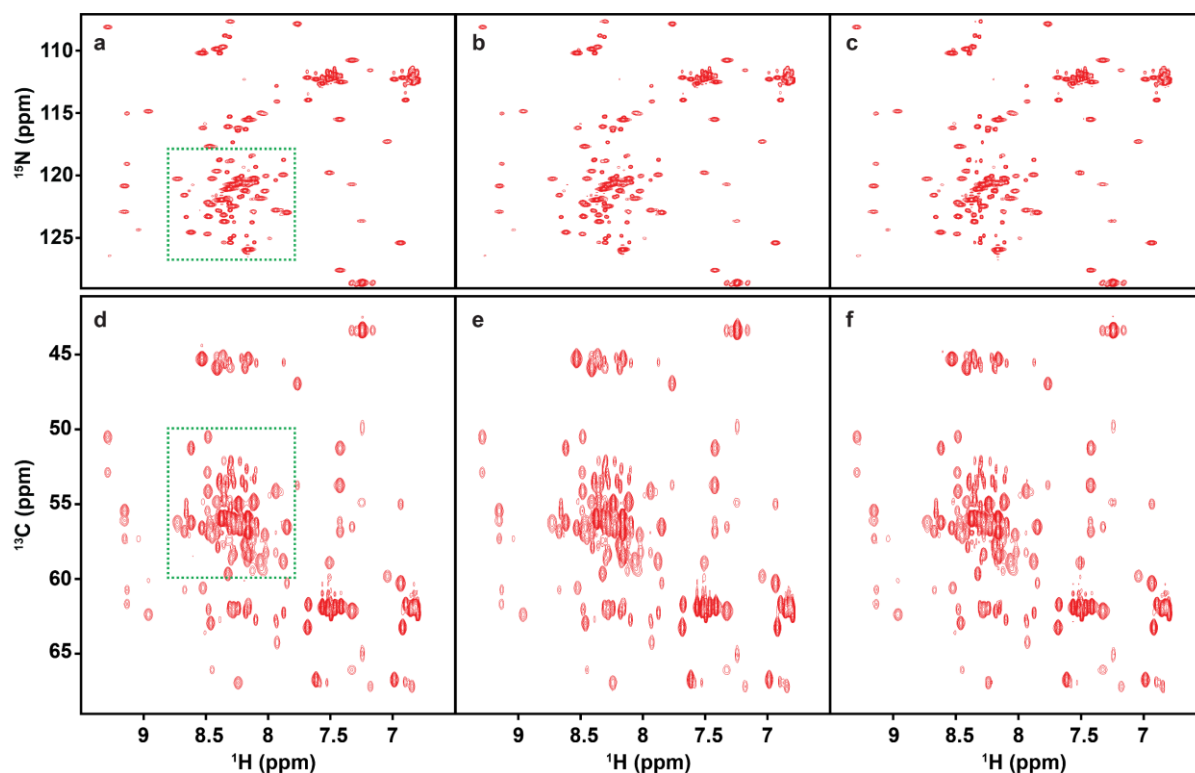
Figure S2-10. The sub-region of the projections on ^{1}H-^{15}N and ^{1}H-^{13}C planes of the 3D HNCACB. (a) and (d) are projection spectra of the fully sampled referenced spectrum. (b) and (e) are projection spectra of the CS reconstructed spectrum. (c) and (f) are projection spectra of the DL reconstructed spectrum. Note: 10% NUS data were acquired for reconstruction. The sub-region of projections marked with green dash rectangle was shown in Figure S2-9.
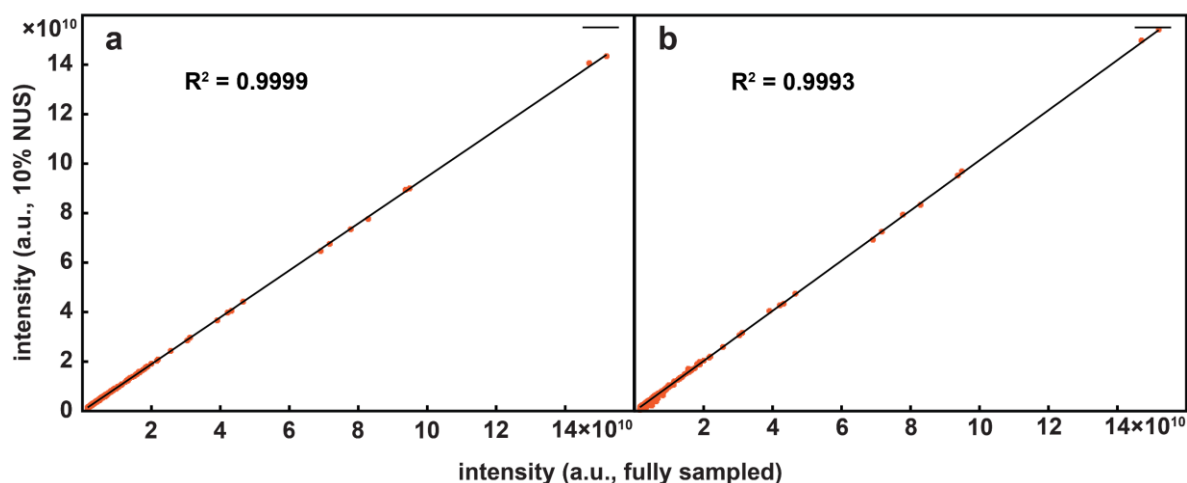

Figure S2-11. Correlation coefficients between reconstructed spectra and fully sampled 3D HNCACB shown in Fig. S2-10. (a) and (b) are the peak intensity correlations achieved by CS and DL, respectively.

References

1. Hoch, J.C. & Stern, A. NMR Data Processing. (Wiley, 1996).
2. Qu, X., Mayzel, M., Cai, J.-F., Chen, Z. & Orekhov, V. *Angew. Chem., Int. Ed.* **54**, 852-854 (2015).
3. Nguyen, H.M., Peng, X., Do, M.N. & Liang, Z. *IEEE Trans. Biomed. Eng.* **60**, 78-89 (2013).
4. Ying, J. et al. *IEEE Trans. Signal Process.* **65**, 3702-3717 (2017).
5. Ying, J. et al. *IEEE Trans. Signal Process.* **66**, 5520-5533 (2018).
6. Huang, G., Liu, Z., Maaten, L.v.d. & Weinberger, K.Q. in *2017 IEEE Conference on Computer Vision and Pattern Recognition (CVPR)* 2261-2269 (IEEE, Honolulu, HI, USA; 2017).
7. Kingma, D. & Ba, J. in *Proceedings of the 3rd International Conference on Learning Representations (ICLR)* (Ithaca, San Diego, CA; 2015).

8. Hyberts, S.G., Milbradt, A.G., Wagner, A.B., Arthanari, H. & Wagner, G. *J. Biomol. NMR.* **52**, 315-327 (2012).

9. Qu, X., Cao, X., Guo, D. & Chen, Z. in *International Society for Magnetic Resonance in Medicine 18th Scientific Meeting (ISMRM)* 3371 (Stockholm, Sweden; 2010).

10. Kazimierczuk, K. & Orekhov, V.Y. *Angew. Chem., Int. Ed.* **50**, 5556-5559 (2011).

11. Qu, X., Guo, D., Cao, X., Cai, S. & Chen, Z. *Sensors.* **11**, 8888-8909 (2011).

12. Delaglio, F. et al. *J. Biomol. NMR.* **6**, 277-293 (1995).

13. Isaksson, L. et al. *PLoS ONE.* **8**, e62947 (2013).

14. Korzhnev, D.M., Karlsson, B.G., Orekhov, V.Y. & Billeter, M. *Protein Sci.* **12**, 56-65 (2003).

15. Kotler, S.A. et al. *Proc. Natl. Acad. Sci. U. S. A.* **116**, 3562-3571 (2019).